VISION-BASED MANIPULATORS NEED TO ALSO SEE FROM THEIR HANDS

Anonymous authors
Paper under double-blind review

ABSTRACT

We study how the choice of visual perspective affects learning and generalization in the context of physical manipulation from raw sensor observations. Compared with the more commonly used global third-person perspective, a hand-centric (eye-in-hand) perspective affords reduced observability, but we find that it consistently improves training efficiency and out-of-distribution generalization. These benefits require no algorithmic changes other than the perspective and hold across a variety of learning algorithms, experimental settings, and distribution shifts, albeit only when hand-centric observability is sufficient. When this is not the case, including a third-person perspective is necessary for learning, but also harms out-of-distribution generalization. To mitigate this, we propose to regularize the third-person information stream via a variational information bottleneck. On six representative manipulation tasks with varying hand-centric observability adapted from the Meta-World benchmark, this simple and broadly applicable principle results in a state-of-the-art reinforcement learning agent operating from both perspectives improving its out-of-distribution generalization on every task.[1]

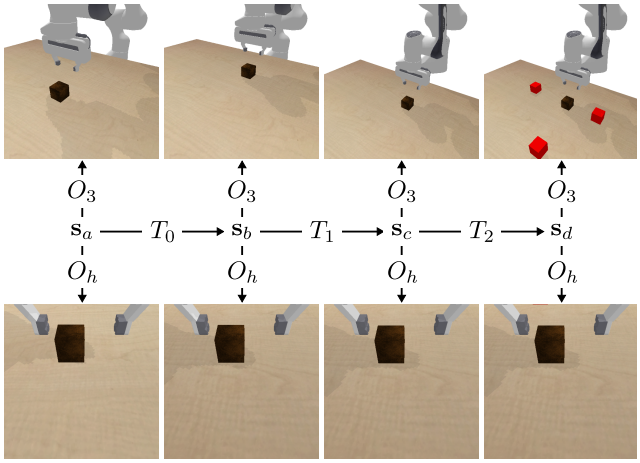

Figure 1: Illustration suggesting the role that visual perspective can play in facilitating the aqcuisition of symmetries with respect to certain transformations on the world state $\mathbf{s}$. T_0: planar translation of the end-effector and cube. T_1: vertical translation of the table surface, end-effector, and cube. T_2: addition of distractor objects. O_3: third-person perspective. O_h: hand-centric perspective.

1 INTRODUCTION

Physical manipulation is so fundamental a skill for natural agents that it has been described as a "Rosetta Stone for cognition" (Ritter & Haschke, 2015). How can we endow machines with similar mastery over their physical environment? One promising avenue is to use a data-driven approach, in which the mapping from raw sensor observations of the environment (and other readily available signals, e.g. via proprioception) to actions is acquired inductively. Helpful inductive biases in modern machine learning techniques such as over-parameterized models and stochastic gradient

[1]Project website: https://sites.google.com/view/seeing-from-hands

descent have enabled surprising (and poorly understood) generalization capabilities in some applications (Neyshabur et al., 2014; Belkin et al., 2019; Zhang et al., 2021). Despite this, visuomotor policies learned end-to-end remain brittle relative to many common real-world distribution shifts: subtle changes in lighting, texture, and geometry that would not faze a human cause drastic performance drops (Julian et al., 2020).

While a wide variety of algorithms have been proposed to improve the learning and generalization of object manipulation skills, in this paper we instead consider the design of the agent's observation space, a facet of the learning pipeline that has been underexplored (Section 5). Indeed, in some applications of machine learning, e.g., image classification or text summarization, the disembodied nature of the task affords relatively little flexibility in this regard. Yet, even in these settings, simple data processing techniques such as normalization and data augmentation can have noticeable effects on learning and generalization (Perez & Wang, 2017). The role of data can only be more profound in an embodied setting: any sensors capable of being practically instrumented will only provide a partial observation of the underlying world state. While partial observability is typically regarded as a challenge that only exacerbates the difficulty of a learning problem (Kaelbling et al., 1998), we may also consider how partial observations can facilitate the acquisition of useful symmetries.

The natural world gives clear examples of this. For instance, because cutaneous touch is inherently restricted to sensing portions of the environment in direct contact with the agent, tactile sensing by construction exhibits invariances to many common transformations on the underlying world state; grasping an apple from the checkout counter (without looking at it) is largely the same as doing so from one's kitchen table. Due in part to the nascent state of tactile sensing hardware (Yuan et al., 2017) and simulation (Agarwal et al., 2020), in this work we investigate the above insight in vision, the ubiquitous robotic sensory modality. In particular, we focus on the role of *perspective* as induced from the placement of cameras. To roughly imitate the locality of cutaneous touch, we consider the hand-centric (eye-in-hand) perspective arising from mounting a camera on a robotic manipulator's wrist. We also consider the more commonly used third-person perspective afforded by a fixed camera in the world frame.

The main contribution of this work is an empirical study of the role of visual perspective in learning and generalization in the context of physical manipulation. We first perform a head-to-head comparison between hand-centric and third-person perspectives in a custom simulated grasping environment that features three kinds of distribution shifts. We find that using the hand-centric perspective, with no other algorithmic modifications, reduces aggregate out-of-distribution failure rate by 92%, 99%, and 100% (relative) in the imitation learning, reinforcement learning, and adversarial imitation learning settings, respectively. We also observe appreciable gains in training efficiency in the latter two settings.

Despite their apparent superiority, hand-centric perspectives cannot be used alone for tasks in which their limited observability is a liability during training. To realize the benefits of hand-centric perspectives more generally, we propose using both hand-centric and third-person perspectives in conjunction for full observability while regularizing the latter with a variational information bottleneck (Alemi et al., 2016) to mitigate the latter's detrimental effects on out-of-distribution generalization. We instantiate this simple and broadly applicable principle in DrQ-v2 (Yarats et al., 2021), a state-of-the-art vision-based reinforcement learning algorithm, and find that it reduces the aggregate out-of-distribution failure rate compared to using both perspectives naively by 64% (relative) across six representative manipulation tasks with varying levels of hand-centric observability adapted from the Meta-World benchmark (Yu et al., 2020).

2 Problem Setup

Preliminaries: MDPs and POMDPs. We frame the physical manipulation tasks considered in this work as discrete-time infinite-horizon Markov decision processes (MDPs). An MDP $\mathcal{M}$ is a 6-tuple $(\mathcal{S}, \mathcal{A}, P, R, \gamma, \mu)$, where $\mathcal{S}$ is a set of states, $\mathcal{A}$ is a set of actions, $P : \mathcal{S} \times \mathcal{A} \to \Pi(\mathcal{S})$ is a state-transition (or dynamics) function, $R : \mathcal{S} \times \mathcal{A} \to \mathbb{R}$ is a reward function, $\gamma \in (0, 1)$ is a discount factor, and $\mu \in \Pi(\mathcal{S})$ is an initial state distribution. An MDP whose state cannot be directly observed can be formalized as a partially observable MDP (POMDP), an 8-tuple $(\mathcal{S}, \mathcal{A}, P, R, \gamma, \mu, \Omega, O)$ that extends the underlying MDP with two ingredients: a set of observations Ω and an observation function $O : \mathcal{S} \times \mathcal{A} \to \Pi(\Omega)$. We consider only a restricted class of POMDPs in which the observation function is limited to be $O : \mathcal{S} \to \Omega$. To solve a POMDP, we optimize a policy

$\pi : \Omega \to \Pi(\mathcal{A})$ to maximize the expected return $\boldsymbol{R}(\mathcal{M}, \pi \circ O) = \mathbb{E}_{\mu,P,\pi}\left[\sum_{t=0}^{\infty} \gamma^t R(s_t, a_t)\right]$, where $\pi \circ O$ maps a state to an action distribution via composing the policy and observation function.

Observation functions. In this work, we denote the observation functions corresponding to the hand-centric and third-person perspectives as O_h and O_3, respectively. We also consider proprioception via forward kinematics, denoting this as O_p. Often, multiple observation functions are used together; for example, we denote using both the hand-centric and proprioceptive observations as O_{h+p}.

Invariances and generalization. We say that a function $f : \mathcal{X} \times \mathcal{Y} \to \mathcal{Z}$ is invariant in domain subspace $\mathcal{X}$ to a transformation $T : \mathcal{X} \to \mathcal{X}$ iff $\forall x \in \mathcal{X}, y \in \mathcal{Y}.\, f(T(x), y) = f(x, y)$. We formalize the notion of generalization by saying that $\pi \circ O$ generalizes in $\mathcal{M}$ to a distribution shift caused by transformation T iff $\boldsymbol{R}(\mathcal{M}, \pi \circ O)$ is invariant in $\mathcal{M}$ to T. We consider two kinds of generalization: in-distribution and out-of-distribution generalization, also referred to as interpolation and extrapolation. The latter corresponds to the agent generalizing in $\mathcal{M}$ to some specified transformation, and the former is a special case when the transformation is identity. In this work, we limit the scope of the transformations on $\mathcal{M}$ we consider to those acting on the initial state distribution μ through the state set $\mathcal{S}$. A few concrete examples of such transformations are illustrated in Figure 1.

3 Hand-Centric vs. Third-Person Perspectives

The first main hypothesis we investigate is that using the hand-centric perspective O_h instead of the third-person perspective O_3 can significantly improve the learning and generalization of the agent $\pi \circ O$. In this section, we probe this hypothesis in a setting where the hand-centric perspective gives sufficient observability of the scene (we will consider the case when this does not hold in Section 4). See project website `https://sites.google.com/view/seeing-from-hands` for animated visualizations.

3.1 Experimental Setup

We consider a visuomotor grasping task instantiated in PyBullet (Coumans & Bai, 2016–2021). A Franka Emika Panda manipulator is tasked with picking up a specific cube that initially rests on a table. The action space is 4-DoF, consisting of 3-DoF end-effector position control and 1-DoF gripper control. Observation functions include O_h and O_3, which output 84×84 RGB images, and O_p, which outputs 3D end-effector position relative to the robot base, 1D gripper width, and a Boolean contact flag for each of two gripper "fingers".

We use three learning algorithms: imitation learning with dataset aggregation (DAgger) (Ross et al., 2011), reinforcement learning using data-regularized Q-functions (DrQ) (Kostrikov et al., 2020), and adversarial imitation learning using discriminator-actor-critic (DAC) (Kostrikov et al., 2018). We defer exposition on these algorithms to Appendix A.2. We run DAgger and DrQ on three experiment variants each targeting a different distribution shift (detailed and visualized in Appendix A.1). With DAC, we assess in-distribution generalization in the training environment and out-of-distribution generalization between demonstration (demo) collection and the training environment. Further details on the model architectures and hyperparameters used can be found in Appendices A.3 and A.4.

3.2 Experimental Results and Discussion

DAgger and DrQ results are reported in Figure 2 and aggregated in Table 1. DAC results are reported in Figure 3, with experiment variant descriptions in the caption.

For DAgger (left two columns of Figure 2), we find that the hand-centric perspective leads to clear improvements in out-of-distribution generalization (test) across all three experiment variants despite in-distribution generalization progress (train) being essentially identical between $\pi \circ O_{h+p}$ and $\pi \circ O_{3+p}$. The only exceptions to $\pi \circ O_{h+p}$ generalizing better are in some instances of the distractor objects variant. Here, seeing the red, green, and blue distractor objects during training was sufficient for both $\pi \circ O_{h+p}$ and $\pi \circ O_{3+p}$ to learn to ignore these object colors, even under distractor distribution shift. Generalization to white distractors was likely facilitated by the RGB representation of white as the "sum" of red, green, and blue.

Table 1: Aggregate cube grasping out-of-distribution generalization performance computed from taking the three highest success rates achieved in each run of each DAgger or DrQ agent across the three experiment variants. The hand-centric perspective leads to the best aggregate success rate for both algorithms, with its 95% confidence intervals of the interquartile mean (IQM) not overlapping those of the third-person perspective. IQM is recommended by Agarwal et al. (2021) when reporting aggregate performance due to its greater robustness to outliers than the mean and better statistical efficiency than the median.

		success rate (%)			
		mean	median	IQM	95% CI of IQM
DAgger	$\pi \circ O_{h+p}$	**92.2**	**99.4**	**97.5**	$[\mathbf{97.0}, \mathbf{97.8}]$
	$\pi \circ O_{3+p}$	64.4	61.1	69.3	$[67.0, 71.4]$
DrQ	$\pi \circ O_{h+p}$	**94.7**	**100.0**	**99.3**	$[\mathbf{98.4}, \mathbf{99.9}]$
	$\pi \circ O_{3+p}$	46.6	59.4	46.9	$[44.3, 49.3]$

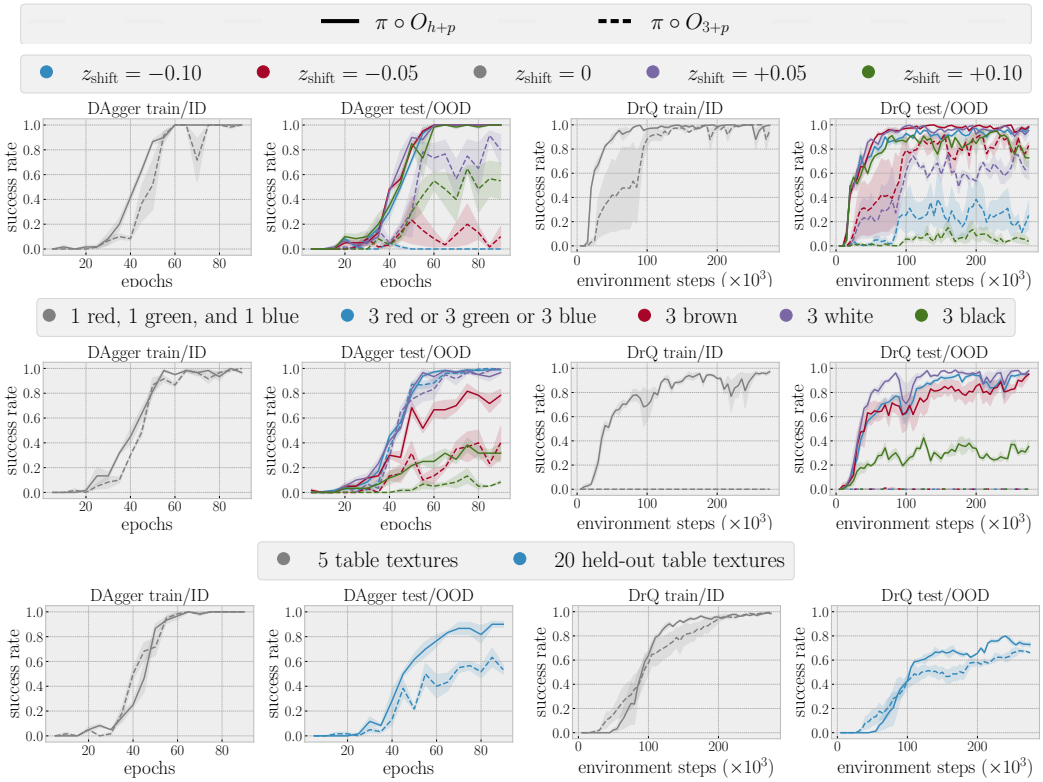

Figure 2: DAgger and DrQ results for cube grasping. The first, second, and third rows respectively contain results for the table height, distractor objects, and table textures experiment variants. See Appendix A.1 for visualizations of the train and test distributions for each experiment variant. Compared to the third-person perspective (dashed lines), the hand-centric perspective (solid lines) leads to better out-of-distribution generalization performance across all three distribution shifts for both DAgger and DrQ. For DrQ, we also see appreciable improvements in sample efficiency when using the hand-centric perspective. Shaded regions indicate the standard error of the mean over three random seeds.

For DrQ (right two columns of Figure 2), the differences between $\pi \circ O_{h+p}$ and $\pi \circ O_{3+p}$ extend into training time. In the table height variant, $\pi \circ O_{h+p}$ exhibits increased sample efficiency for training as well as similar out-of-distribution generalization benefits as seen for DAgger. For the distractor objects variant, $\pi \circ O_{h+p}$ converges before $\pi \circ O_{3+p}$ makes any significant progress on success rate (though we did observe increasing returns). Since DrQ trained $\pi \circ O_{3+p}$ to convergence for the other variants within the same interaction budget, it follows that the presence of the distractors rendered the training task too hard for $\pi \circ O_{3+p}$, but not for $\pi \circ O_{h+p}$. In the table textures variant, the generalization improvement of $\pi \circ O_{h+p}$ over $\pi \circ O_{3+p}$ is less extreme. We attribute this to invariances to image-space transformations learned via the data augmentation built into the DrQ algorithm.

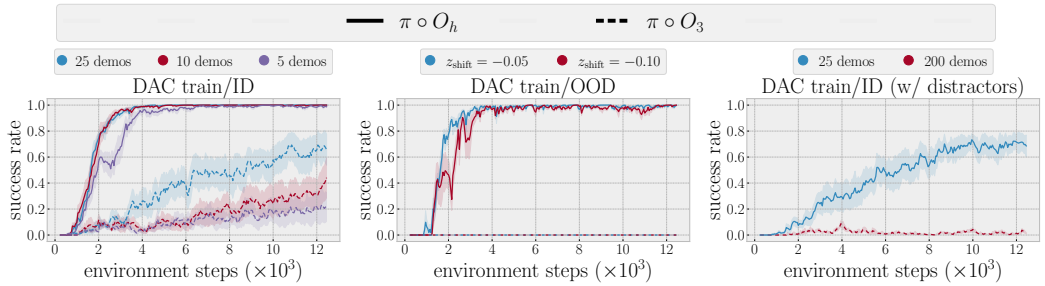

Figure 3: DAC results for cube grasping. Left: base variant (initial object and end-effector position randomization) with no distribution shift between demo collection and training. Center: base variant with table height shift between collection of 25 demos and training. Right: base variant plus three distractor objects with no distribution shift between demo collection and training. Across the three experiment variants, the hand-centric perspective enables the agent to generalize in- and out-of-distribution more efficiently and effectively. Shaded regions indicate the standard error of the mean over five random seeds.

For DAC, we find stark improvements in the generalization of $\pi \circ O_h$ over that of $\pi \circ O_3$. In the first DAC-specific experiment variant (left plot of Figure 3), $\pi \circ O_h$ fully generalizes in-distribution with as few as 5 demos, whereas $\pi \circ O_3$ achieves significantly lower success, even with 25 demos and much more online interaction. In the second variant (center plot of Figure 3), the distribution shift between demo collection and training barely affects $\pi \circ O_h$, but severely compromises the training of $\pi \circ O_3$. In the third variant (right plot of Figure 3), despite the presence of distractor objects giving the discriminator strong predictive power in distinguishing between demos and agent behavior, $\pi \circ O_h$ still achieves a significant measure of in-distribution generalization, whereas $\pi \circ O_3$ makes little progress even with eight times the number of demos. We remark that, in the context of adversarial imitation learning, $\pi \circ O_h$ achieves its sample efficiency and robustness without any special requirements on the training data (Zolna et al., 2020) or modified training objectives (Xu & Denil, 2020).

4 Combining Hand-Centric and Third-Person Perspectives

The previous set of experiments demonstrate how hand-centric perspectives can lead to clear improvements in learning and generalization over third-person perspectives. Unfortunately, this does not mean that the use of hand-centric perspectives is a panacea. The limited observability of hand-centric perspectives is a double-edged sword: depending on the environment and task, it can enable $\pi \circ O_h$ to establish useful invariances, or confuse $\pi \circ O_h$ by enforcing harmful ones. In this section, we focus on evaluating across tasks of varying hand-centric observability, including those in which insufficient observability severely undermines $\pi \circ O_h$. How can we realize the benefits of hand-centric perspectives even in such scenarios?

4.1 Regularizing the Third-Person Information Stream

Insufficient observability arising from using O_h alone necessitates the inclusion of O_3. While using both perspectives should effectively resolve the issue of insufficient observability and enable the agent to train, we know from Section 3.2 that the use of the third-person perspective can hamper out-of-distribution generalization by allowing the agent to "overfit" to particularities of the training distribution. To mitigate this, we propose to regularize the third-person perspective's representation. While multiple regularization techniques could conceivably be suitable to this end, we choose the variational information bottleneck (VIB) to use in our experiments due to its simplicity, theoretical justification, and empirical performance (Alemi et al., 2016).

For our subsequent experiments, we build on top of the state-of-the-art vision-based actor-critic reinforcement learning algorithm DrQ-v2 (Yarats et al., 2021) (see Appendix B.3 for a detailed description). When we use both hand-centric and third-person observations $\mathbf{o}_h$ and $\mathbf{o}_3$, we instantiate two separate image encoders f_{ξ_h} and f_{ξ_3}. We denote the corresponding representations as $\mathbf{z}_h$ and $\mathbf{z}_3$. These are concatenated before being fed to the actor π_ϕ and critic networks $Q_{\theta_1}, Q_{\theta_2}$.

We apply a VIB to the third-person information stream to regularize the DrQ-v2 critic. This amounts to a variational approximation to maximizing the mutual information between the third-person ob-

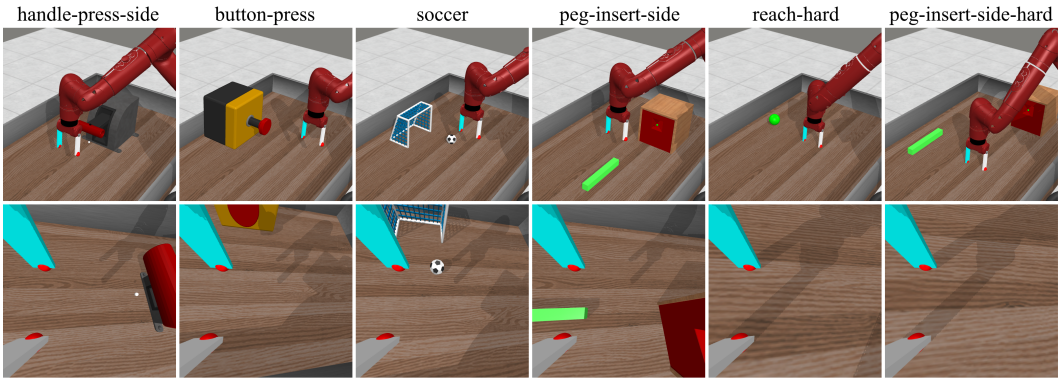

Figure 4: The Meta-World tasks used in the experiments in Section 4. The top row contains third-person observations $\mathbf{o}_3$, and the bottom row contains corresponding hand-centric observations $\mathbf{o}_h$. Initial object positions are randomized. The last two tasks, reach-hard and peg-insert-side-hard, are custom-made; there, the green goal and the green peg are randomly initialized either to the left or to the right of the gripper with equal probability, and they are not initially visible to the hand-centric perspective. Because of the severely limited hand-centric observability, the third-person perspective is crucial for learning to direct the gripper to the correct location. This is especially the case for the reach-hard task, which we modified to prohibit any vertical end-effector movement. See Section B.1 in the Appendix for more details about each task.

servations and the critic's predictions of the temporal difference targets while minimizing the mutual information between the third-person observations and their representations. We implement this by replacing the deterministic third-person encoder f_{ξ_3} with a stochastic encoder $p_{\xi_3}(\mathbf{z}_3|\mathbf{o}_3)$, specifying a prior $p(\mathbf{z}_3)$, and adding a weighted KL divergence term to the critic loss. The VIB-regularized DrQ-v2 critic objective is

$$\mathcal{L}(\xi_h, \xi_3, \theta_1, \theta_2) = \mathbb{E}_{\mathcal{D},\, p_{\xi_3}} \left[\mathcal{L}_{\text{DrQ-v2 critic}}(\xi_h, \xi_3, \theta_1, \theta_2)\right] + \mathbb{E}_{\mathcal{D}} \left[\beta_3 D_{\text{KL}}(p_{\xi_3}(\mathbf{z}_3|\mathbf{o}_3) \parallel p(\mathbf{z}_3))\right], \quad (1)$$

where $\mathcal{D}$ is the replay buffer. We specify $p_{\xi_3}(\mathbf{z}_3|\mathbf{o}_3)$ as a diagonal Gaussian and $p(\mathbf{z}_3)$ as a standard Gaussian, which enables analytical computation of the KL divergence. We use the reparameterization trick to enable optimization of the first term via pathwise derivatives. We do not need to modify the actor objective as only gradients from the critic are used to update the encoder(s) in DrQ-v2. We remark that a (variational) information bottleneck can be applied to many imitation learning and reinforcement learning algorithms (Peng et al., 2018; Goyal et al., 2019; Igl et al., 2019; Kumar et al., 2021).

4.2 Experimental setup

We evaluate the learning and generalization performance of seven DrQ-v2 agents: $\pi \circ O_{h+p}$ (hand-centric perspective), $\pi \circ O_{3+p}$ (third-person perspective), $\pi \circ O_{h+3+p}$ (both perspectives), $\pi \circ O_{h+3+p} + \text{VIB}(\mathbf{z}_3)$ (both perspectives with a VIB on the third-person information stream), and three ablation agents introduced later. We evaluate the agents on six tasks adapted from the Meta-World benchmark (Yu et al., 2020). We design the task set to exhibit three levels of hand-centric observability (high, moderate, and low) with two tasks per level.

In every Meta-World task, a simulated Sawyer robot manipulates objects resting on a table. The action space is 4-DoF, consisting of 3-DoF end-effector position control and 1-DoF gripper control. We do not use the original Meta-World observation space as it contains low-dimensional pose information about task-pertinent objects instead of images. Rather, we configure the observations so that O_h and O_3 output 84×84 RGB images, and O_p outputs 3D end-effector position and 1D gripper width. See Figure 4 for a visualization of each task through the lens of O_h and O_3.

While the distribution shifts in the experiments of the previous section arise from transformations on the table height, distractor objects, and table textures, in this section we focus on distribution shifts arising from transformations on the initial object positions. All object positions have disjoint initial train and test distributions such that the latter's support "surrounds" that of the former (see Table 7 in Appendix B.2 for details).

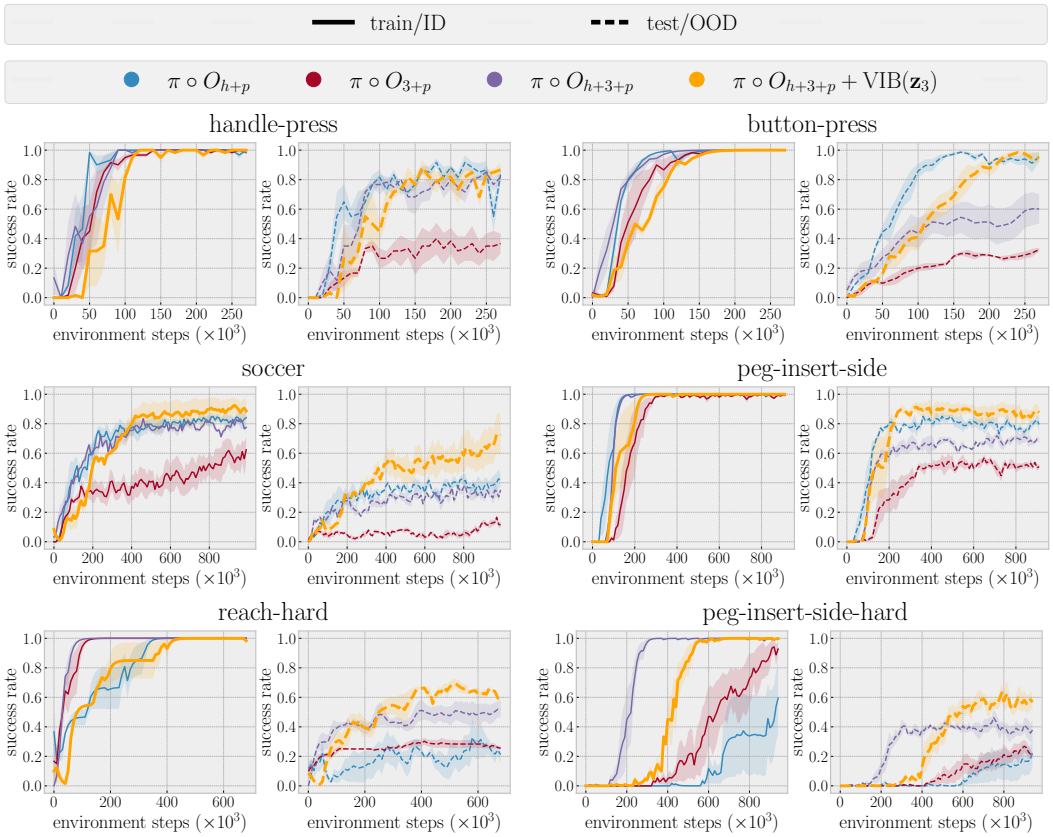

Figure 5: DrQ-v2 results for Meta-World. Each row contains results for two manipulation tasks that roughly exhibit the same level of hand-centric observability, which decreases from top to bottom (high, moderate, low). Using the proposed approach (both perspectives with a VIB on the third-person perspective's representation) leads to the best out-of-distribution generalization performance for all levels of hand-centric observability (though it is matched by the hand-centric perspective when hand-centric observability is high, as expected). Shaded regions indicate the standard error of the mean over three random seeds.

Aside from adapting the DrQ-v2 algorithm to our setting as described above, we use the original DrQ-v2 model and hyperparameters with some minor exceptions (see Appendix B.5 for details). Hyperparameters that are common to all agents are shared for a given task. With agents that include regularization, we tune the regularization weight(s) on a validation sample from the test distribution. Test success rate is computed on a separate sample of 20 environments from the test distribution.

4.3 Experimental results and discussion

Main experimental results in Meta-World are presented in Figure 5. Results for ablation studies on $\pi \circ O_{h+3+p} + \text{VIB}(\mathbf{z}_3)$ are presented in Figure 11 in Appendix B.4 due to space constraints. Table 2 summarizes all results, including ablations. When using both perspectives, regularizing the third-person perspective's representation via a VIB reduces the interquartile mean of the out-of-distribution failure rate across all six tasks by 64%. We also note that this method achieves the best performance in each individual task, albeit sometimes with less sample efficiency. To properly explain these phenomena, we now embark on a more stratified analysis and discussion of the results.

Characterization of hand-centric observability via training performance. When the world state is sufficiently observable via the hand-centric perspective, we expect the convergence during training of $\pi \circ O_{h+p}$ to match or surpass that of $\pi \circ O_{3+p}$. We find that this is indeed the case for handle-press-side, button-press, soccer, and peg-insert-side (high and moderate hand-centric observability), and not the case for reach-hard or peg-insert-side-hard (low hand-centric observability). This validates our selection and framing of the tasks at different levels of hand-centric observability.

Table 2: Aggregate out-of-distribution generalization performance computed from taking the three highest success rates achieved in each run of each DrQ-v2 agent across all six Meta-World tasks. Using both perspectives with a VIB on the third-person perspective's representation results in the best aggregate success rate, with its 95% confidence intervals of the interquartile mean (IQM) not overlapping those of any other method.

	success rate (%)			
	mean	median	IQM	95% CI of IQM
$\pi \circ O_{h+p}$	69.6	73.1	73.7	$[72.1, 75.4]$
$\pi \circ O_{3+p}$	55.6	51.7	56.6	$[53.4, 59.1]$
$\pi \circ O_{h+3+p}$	67.4	68.1	66.3	$[62.9, 69.8]$
$\pi \circ O_{h+3+p} + \text{VIB}(\mathbf{z}_3)$	**84.4**	**82.5**	**87.7**	$[\mathbf{85.2}, \mathbf{90.0}]$
$\pi \circ O_{h+3+p} + \text{VIB}(\mathbf{z}_h) + \text{VIB}(\mathbf{z}_3)$	51.8	54.7	58.2	$[50.5, 65.9]$
$\pi \circ O_{3'+3+p} + \text{VIB}(\mathbf{z}_3)$	40.6	32.8	34.5	$[32.7, 36.4]$
$\pi \circ O_{h+3+p} + \ell_2(\mathbf{z}_3)$	70.3	70.0	69.8	$[67.7, 72.3]$

Hand-centric perspective vs. third-person perspective. When hand-centric observability is high or moderate, $\pi \circ O_{h+p}$ generalizes better out-of-distribution than $\pi \circ O_{3+p}$, corroborating results from Section 3.2 with another form of distribution shift. When hand-centric observability is low, $\pi \circ O_{h+p}$ both trains and generalizes worse than $\pi \circ O_{3+p}$. This supports our motivation for considering using both perspectives in conjunction.

Effect of combining the hand-centric and third-person perspectives. When hand-centric observability is high or moderate, including the third-person perspective can harm generalization. We see that for button-press, peg-insert-side, handle-press-side, and soccer, $\pi \circ O_{h+3+p}$ is sandwiched between $\pi \circ O_{h+p}$ and $\pi \circ O_{3+p}$ on the test distribution. The drop from $\pi \circ O_{h+p}$ to $\pi \circ O_{h+3+p}$ is significant for the former two tasks, and marginal for the latter two. This validates our hypothesis that including O_3 enables the agent to "overfit" to training conditions. When hand-centric observability is low, combining both perspectives results in $\pi \circ O_{h+3+p}$ matching or surpassing the training performance of $\pi \circ O_{h+p}$ and $\pi \circ O_{3+p}$, and greatly outperforming both at test time. This validates our hypothesis that, when necessary, including third-person observations helps resolve training difficulties arising from insufficient hand-centric observability.

Effect of regularizing the third-person information stream via a VIB. $\pi \circ O_{h+3+p} + \text{VIB}(\mathbf{z}_3)$ consistently improves upon $\pi \circ O_{h+3+p}$ in out-of-distribution generalization for all tasks except handle-press-side, in which the two are about equal. This directly indicates the benefit of the VIB regularization. These gains come at the cost of slightly delaying the convergence of training. However, it is arguable that this is inevitable and even desirable. A known phenomenon in neural network training is that spurious correlations or "shortcuts" in the data are sometimes easier to learn than causal relationships (Sagawa et al., 2019). Slower training and higher generalization may indicate the avoidance of such behavior. Additionally, in button-press, $\pi \circ O_{h+3+p} + \text{VIB}(\mathbf{z}_3)$ recovers the out-of-distribution generalization exhibited by $\pi \circ O_{h+p}$, and when hand-centric observability is moderate, $\pi \circ O_{h+3+p} + \text{VIB}(\mathbf{z}_3)$ improves upon $\pi \circ O_{h+p}$.

To better understand what makes $\pi \circ O_{h+3+p} + \text{VIB}(\mathbf{z}_3)$ work the best, we also conduct three ablation studies. Curves for the ablation studies are presented in Figure 11 in the Appendix.

What if both perspectives are regularized? The ablation agent $\pi \circ O_{h+3+p} + \text{VIB}(\mathbf{z}_h) + \text{VIB}(\mathbf{z}_3)$ adds a separate VIB to the hand-centric information stream in an analogous manner to how the third-person perspective's representation is regularized (detailed in Section 4.1). We use the same β_3 for both and tune β_h. Note that setting $\beta_h = 0$ for $\pi \circ O_{h+3+p} + \text{VIB}(\mathbf{z}_h) + \text{VIB}(\mathbf{z}_3)$ recovers $\pi \circ O_{h+3+p} + \text{VIB}(\mathbf{z}_3)$ modulo stochasticity in $\mathbf{z}_h$, so we limit the lowest value β_h can take to 0.01. We find that in no task does $\pi \circ O_{h+3+p} + \text{VIB}(\mathbf{z}_h) + \text{VIB}(\mathbf{z}_3)$ outperform $\pi \circ O_{h+3+p} + \text{VIB}(\mathbf{z}_3)$, validating our choice of only regularizing the third-person perspective's representation.

Assessing the importance of the hand-centric perspective. $\pi \circ O_{3'+3+p} + \text{VIB}(\mathbf{z}_3)$ uses a second third-person perspective $O_{3'}$ instead of the hand-centric perspective O_h. Visualizations from this additional third-person perspective are shown in Figure 12 in Appendix B.4. We re-tune β_3 for this agent. We find that $\pi \circ O_{3'+3+p} + \text{VIB}(\mathbf{z}_3)$ performs significantly worse than $\pi \circ O_{h+3+p} + \text{VIB}(\mathbf{z}_3)$, affirming the benefit of using the hand-centric perspective in the multi-perspective setting.

$\mathbf{z}_h$-dependent regularization of $\mathbf{z}_3$. $\text{VIB}(\mathbf{z}_3)$ reduces the information contained in $\mathbf{z}_3$ without directly considering $\mathbf{z}_h$. With the ablation agent $\pi \circ O_{h+3+p} + \ell_2(\mathbf{z}_3)$, we consider a simple form of $\mathbf{z}_h$-dependent regularization of $\mathbf{z}_3$ in which we push $\mathbf{z}_3$ towards $\mathbf{z}_h$ by adding a weighted regularization term $\alpha_3 \|\mathbf{z}_3 - \text{stopgrad}(\mathbf{z}_h)\|_2^2$ to the DrQ-v2 critic objective. This approach seems promising given that $\pi \circ O_{h+3+p}$ consistently outperforms $\pi \circ O_{3+p}$ across all six tasks, suggesting that even in the midst of substantial partial observability, $\mathbf{z}_h$ may represent information in a useful and generalizable way. We tune α_3. We find that $\pi \circ O_{h+3+p} + \ell_2(\mathbf{z}_3)$ marginally improves over vanilla $\pi \circ O_{h+3+p}$ but still comes far short of $\pi \circ O_{h+3+p} + \text{VIB}(\mathbf{z}_3)$, suggesting that the two perspectives contain important complementary information that is better represented separately.

5 Related Work

Learning for vision-based object manipulation. A wide range of works have focused on algorithmic development for end-to-end learning of vision-based object manipulation skills (Levine et al., 2016; Agrawal et al., 2016; Finn et al., 2016; 2017; Kalashnikov et al., 2018; Srinivas et al., 2018; Ebert et al., 2018; Zhu et al., 2018; Jayaraman et al., 2018; Rafailov et al., 2021). Some works on learned visuomotor control use eye-in-hand cameras for tasks such as grasping (Song et al., 2020) and insertion (Zhao et al., 2020; Luo et al., 2021), and others which pre-date end-to-end visuomotor learning use both eye-in-hand and third-person cameras for visual servoing (Flandin et al., 2000; Lippiello et al., 2005). Very few works consider the design of camera placements (Zaky et al., 2020) or conduct any controlled comparisons on different combinations of visual perspectives (Mandlekar et al., 2021; Wu et al., 2021). Unlike all of these works, we propose specific hypotheses regarding the benefits of different choices of visual perspective and perform a detailed empirical validation of these hypotheses with evaluation on multiple families of learning algorithms, manipulation tasks, and distribution shifts.

The role of perspective in multimodal interactive navigation. Hill et al. (2019) assess an agent learning to execute language instructions in simulated environments using high-level actions and find that using an egocentric observation space results in better systematic generalization to new instruction noun-verb combinations. While our work similarly investigates the effect of visual perspective on learning and generalization, their main controlled comparisons in supporting the above claim are done in a 2D grid-world. In contrast, our work focuses on vision-based physical manipulation tasks, and we investigate how to maintain the benefits of locality while mitigating the associated pitfalls of insufficient observability without resorting to memory.

Invariances through data augmentation in reinforcement learning. Several works have investigated ways to apply standard data augmentation techniques from computer vision in the reinforcement learning setting. Laskin et al. (2020) demonstrate the efficacy of doing so on a wide range of environments and algorithms, while Kostrikov et al. (2020) and Yarats et al. (2021) regularize the action-value function in soft actor-critic (Haarnoja et al., 2018) and deep deterministic policy gradients (Lillicrap et al., 2015) via these techniques. These works consider data augmentation as a means to prescribe invariances to image-space transformations, whereas we are concerned with how different observation functions facilitate generalization to environmental transformations. To emphasize that these directions are orthogonal, we use DrQ and DrQ-v2 (the algorithms proposed by Kostrikov et al. (2020) and Yarats et al. (2021)) in our experiments. However, these works and ours are broadly related in that they propose practically simple modifications on the data that yield noticeable benefits with little or no algorithmic change.

6 Conclusion

In this work, we focus on empirically studying an underexplored design choice in the embodied learning pipeline: the observation function. While robotic hand-centric perception is more traditionally instrumented with tactile sensing, our findings affirm that perspective, even when controlling for modality, can play an important role in learning and generalization. Overall, in the context of end-to-end learning for visuomotor policies, our findings lead us to recommend using hand-centric perspectives when their limited observability is sufficient, and otherwise defaulting to using both hand-centric and third-person perspectives while regularizing the representation of the latter. The breadth of the learning algorithms, manipulation tasks, and distribution shifts that we base these conclusions on, coupled with their simplicity and lack of restrictive assumptions, suggests that these recommendations should be broadly applicable.

REPRODUCIBILITY STATEMENT

Sections 3.1 and 4.2 give overviews of the experimental setup, and Appendices A and B flesh out the full experimental protocol in stringent detail. We expect this to be sufficient for independent replication of our main findings. Separately, for the sake of reproduction, we will also release code for all experiments upon publication.

REFERENCES

Arpit Agarwal, Tim Man, and Wenzhen Yuan. Simulation of vision-based tactile sensors using physics based rendering. *arXiv preprint arXiv:2012.13184*, 2020.

Rishabh Agarwal, Max Schwarzer, Pablo Samuel Castro, Aaron Courville, and Marc G Bellemare. Deep reinforcement learning at the edge of the statistical precipice. *arXiv preprint arXiv:2108.13264*, 2021.

Pulkit Agrawal, Ashvin Nair, Pieter Abbeel, Jitendra Malik, and Sergey Levine. Learning to poke by poking: Experiential learning of intuitive physics. *arXiv preprint arXiv:1606.07419*, 2016.

Alexander A Alemi, Ian Fischer, Joshua V Dillon, and Kevin Murphy. Deep variational information bottleneck. *arXiv preprint arXiv:1612.00410*, 2016.

Mikhail Belkin, Daniel Hsu, Siyuan Ma, and Soumik Mandal. Reconciling modern machine-learning practice and the classical bias–variance trade-off. *Proceedings of the National Academy of Sciences*, 116(32):15849–15854, 2019.

Mircea Cimpoi, Subhransu Maji, Iasonas Kokkinos, Sammy Mohamed, and Andrea Vedaldi. Describing textures in the wild. In *Proceedings of the IEEE Conference on Computer Vision and Pattern Recognition*, pp. 3606–3613, 2014.

Erwin Coumans and Yunfei Bai. Pybullet, a python module for physics simulation for games, robotics and machine learning. http://pybullet.org, 2016–2021.

Frederik Ebert, Chelsea Finn, Sudeep Dasari, Annie Xie, Alex Lee, and Sergey Levine. Visual foresight: Model-based deep reinforcement learning for vision-based robotic control. *arXiv preprint arXiv:1812.00568*, 2018.

Chelsea Finn, Xin Yu Tan, Yan Duan, Trevor Darrell, Sergey Levine, and Pieter Abbeel. Deep spatial autoencoders for visuomotor learning. In *2016 IEEE International Conference on Robotics and Automation (ICRA)*, pp. 512–519. IEEE, 2016.

Chelsea Finn, Tianhe Yu, Tianhao Zhang, Pieter Abbeel, and Sergey Levine. One-shot visual imitation learning via meta-learning. In *Conference on Robot Learning*, pp. 357–368. PMLR, 2017.

Grégory Flandin, François Chaumette, and Eric Marchand. Eye-in-hand/eye-to-hand cooperation for visual servoing. In *Proceedings 2000 ICRA. Millennium Conference. IEEE International Conference on Robotics and Automation. Symposia Proceedings (Cat. No. 00CH37065)*, volume 3, pp. 2741–2746. IEEE, 2000.

Scott Fujimoto, Herke Hoof, and David Meger. Addressing function approximation error in actor-critic methods. In *International Conference on Machine Learning*, pp. 1587–1596. PMLR, 2018.

Anirudh Goyal, Riashat Islam, Daniel Strouse, Zafarali Ahmed, Matthew Botvinick, Hugo Larochelle, Yoshua Bengio, and Sergey Levine. Infobot: Transfer and exploration via the information bottleneck. *arXiv preprint arXiv:1901.10902*, 2019.

Tuomas Haarnoja, Aurick Zhou, Pieter Abbeel, and Sergey Levine. Soft actor-critic: Off-policy maximum entropy deep reinforcement learning with a stochastic actor. In *International conference on machine learning*, pp. 1861–1870. PMLR, 2018.

Kaiming He, Xiangyu Zhang, Shaoqing Ren, and Jian Sun. Deep residual learning for image recognition. In *Proceedings of the IEEE conference on computer vision and pattern recognition*, pp. 770–778, 2016.

Felix Hill, Andrew Lampinen, Rosalia Schneider, Stephen Clark, Matthew Botvinick, James L McClelland, and Adam Santoro. Environmental drivers of systematicity and generalization in a situated agent. *arXiv preprint arXiv:1910.00571*, 2019.

Jonathan Ho and Stefano Ermon. Generative adversarial imitation learning. In *Advances in Neural Information Processing Systems*, 2016.

Maximilian Igl, Kamil Ciosek, Yingzhen Li, Sebastian Tschiatschek, Cheng Zhang, Sam Devlin, and Katja Hofmann. Generalization in reinforcement learning with selective noise injection and information bottleneck. *arXiv preprint arXiv:1910.12911*, 2019.

Dinesh Jayaraman, Frederik Ebert, Alexei A Efros, and Sergey Levine. Time-agnostic prediction: Predicting predictable video frames. *arXiv preprint arXiv:1808.07784*, 2018.

Ryan Julian, Benjamin Swanson, Gaurav S Sukhatme, Sergey Levine, Chelsea Finn, and Karol Hausman. Never stop learning: The effectiveness of fine-tuning in robotic reinforcement learning. *arXiv preprint arXiv:2004.10190*, 2020.

Leslie Pack Kaelbling, Michael L Littman, and Anthony R Cassandra. Planning and acting in partially observable stochastic domains. *Artificial intelligence*, 101(1-2):99–134, 1998.

Dmitry Kalashnikov, Alex Irpan, Peter Pastor, Julian Ibarz, Alexander Herzog, Eric Jang, Deirdre Quillen, Ethan Holly, Mrinal Kalakrishnan, Vincent Vanhoucke, et al. Qt-opt: Scalable deep reinforcement learning for vision-based robotic manipulation. *arXiv preprint arXiv:1806.10293*, 2018.

Ilya Kostrikov, Kumar Krishna Agrawal, Debidatta Dwibedi, Sergey Levine, and Jonathan Tompson. Discriminator-actor-critic: Addressing sample inefficiency and reward bias in adversarial imitation learning. *arXiv preprint arXiv:1809.02925*, 2018.

Ilya Kostrikov, Denis Yarats, and Rob Fergus. Image augmentation is all you need: Regularizing deep reinforcement learning from pixels. *arXiv preprint arXiv:2004.13649*, 2020.

Aviral Kumar, Anikait Singh, Stephen Tian, Chelsea Finn, and Sergey Levine. A workflow for offline model-free robotic reinforcement learning. *arXiv preprint arXiv:2109.10813*, 2021.

Michael Laskin, Kimin Lee, Adam Stooke, Lerrel Pinto, Pieter Abbeel, and Aravind Srinivas. Reinforcement learning with augmented data. *arXiv preprint arXiv:2004.14990*, 2020.

Sergey Levine, Chelsea Finn, Trevor Darrell, and Pieter Abbeel. End-to-end training of deep visuomotor policies. *The Journal of Machine Learning Research*, 17(1):1334–1373, 2016.

Timothy P Lillicrap, Jonathan J Hunt, Alexander Pritzel, Nicolas Heess, Tom Erez, Yuval Tassa, David Silver, and Daan Wierstra. Continuous control with deep reinforcement learning. *arXiv preprint arXiv:1509.02971*, 2015.

Vincenzo Lippiello, Bruno Siciliano, and Luigi Villani. Eye-in-hand/eye-to-hand multi-camera visual servoing. In *Proceedings of the 44th IEEE Conference on Decision and Control*, pp. 5354–5359. IEEE, 2005.

Jianlan Luo, Oleg Sushkov, Rugile Pevceviciute, Wenzhao Lian, Chang Su, Mel Vecerik, Ning Ye, Stefan Schaal, and Jon Scholz. Robust multi-modal policies for industrial assembly via reinforcement learning and demonstrations: A large-scale study. *arXiv preprint arXiv:2103.11512*, 2021.

Ajay Mandlekar, Danfei Xu, Josiah Wong, Soroush Nasiriany, Chen Wang, Rohun Kulkarni, Li Fei-Fei, Silvio Savarese, Yuke Zhu, and Roberto Martín-Martín. What matters in learning from offline human demonstrations for robot manipulation. *arXiv preprint arXiv:2108.03298*, 2021.

Volodymyr Mnih, Koray Kavukcuoglu, David Silver, Alex Graves, Ioannis Antonoglou, Daan Wierstra, and Martin Riedmiller. Playing atari with deep reinforcement learning. *arXiv preprint arXiv:1312.5602*, 2013.

Behnam Neyshabur, Ryota Tomioka, and Nathan Srebro. In search of the real inductive bias: On the role of implicit regularization in deep learning. *arXiv preprint arXiv:1412.6614*, 2014.

Xue Bin Peng, Angjoo Kanazawa, Sam Toyer, Pieter Abbeel, and Sergey Levine. Variational discriminator bottleneck: Improving imitation learning, inverse rl, and gans by constraining information flow. *arXiv preprint arXiv:1810.00821*, 2018.

Luis Perez and Jason Wang. The effectiveness of data augmentation in image classification using deep learning. *arXiv preprint arXiv:1712.04621*, 2017.

Rafael Rafailov, Tianhe Yu, Aravind Rajeswaran, and Chelsea Finn. Offline reinforcement learning from images with latent space models. In *Learning for Dynamics and Control*, pp. 1154–1168. PMLR, 2021.

Helge Ritter and Robert Haschke. Hands, dexterity, and the brain. *Humanoid robotics and neuroscience: science, engineering and society*, 2015.

Stéphane Ross, Geoffrey Gordon, and Drew Bagnell. A reduction of imitation learning and structured prediction to no-regret online learning. In *Proceedings of the fourteenth international conference on artificial intelligence and statistics*, pp. 627–635. JMLR Workshop and Conference Proceedings, 2011.

Shiori Sagawa, Pang Wei Koh, Tatsunori B Hashimoto, and Percy Liang. Distributionally robust neural networks for group shifts: On the importance of regularization for worst-case generalization. *arXiv preprint arXiv:1911.08731*, 2019.

Shuran Song, Andy Zeng, Johnny Lee, and Thomas Funkhouser. Grasping in the wild: Learning 6dof closed-loop grasping from low-cost demonstrations. *IEEE Robotics and Automation Letters*, 5(3):4978–4985, 2020.

Aravind Srinivas, Allan Jabri, Pieter Abbeel, Sergey Levine, and Chelsea Finn. Universal planning networks: Learning generalizable representations for visuomotor control. In *International Conference on Machine Learning*, pp. 4732–4741. PMLR, 2018.

Bohan Wu, Suraj Nair, Li Fei-Fei, and Chelsea Finn. Example-driven model-based reinforcement learning for solving long-horizon visuomotor tasks. *arXiv preprint arXiv:2109.10312*, 2021.

Danfei Xu and Misha Denil. Positive-unlabeled reward learning. *Conference on Robot Learning*, 2020.

Denis Yarats, Rob Fergus, Alessandro Lazaric, and Lerrel Pinto. Mastering visual continuous control: Improved data-augmented reinforcement learning. *arXiv preprint arXiv:2107.09645*, 2021.

Tianhe Yu, Deirdre Quillen, Zhanpeng He, Ryan Julian, Karol Hausman, Chelsea Finn, and Sergey Levine. Meta-world: A benchmark and evaluation for multi-task and meta reinforcement learning. In *Conference on Robot Learning*, pp. 1094–1100. PMLR, 2020.

Wenzhen Yuan, Siyuan Dong, and Edward H Adelson. Gelsight: High-resolution robot tactile sensors for estimating geometry and force. *Sensors*, 17(12):2762, 2017.

Youssef Zaky, Gaurav Paruthi, Bryan Tripp, and James Bergstra. Active perception and representation for robotic manipulation. *arXiv preprint arXiv:2003.06734*, 2020.

Chiyuan Zhang, Samy Bengio, Moritz Hardt, Benjamin Recht, and Oriol Vinyals. Understanding deep learning (still) requires rethinking generalization. *Communications of the ACM*, 64(3):107–115, 2021.

Tony Z Zhao, Anusha Nagabandi, Kate Rakelly, Chelsea Finn, and Sergey Levine. Meld: Meta-reinforcement learning from images via latent state models. *arXiv preprint arXiv:2010.13957*, 2020.

Yuke Zhu, Ziyu Wang, Josh Merel, Andrei Rusu, Tom Erez, Serkan Cabi, Saran Tunyasuvunakool, János Kramár, Raia Hadsell, Nando de Freitas, et al. Reinforcement and imitation learning for diverse visuomotor skills. *arXiv preprint arXiv:1802.09564*, 2018.

Konrad Zolna, Scott Reed, Alexander Novikov, Sergio Gomez Colmenarejo, David Budden, Serkan Cabi, Misha Denil, Nando de Freitas, and Ziyu Wang. Task-relevant adversarial imitation learning. *Conference on Robot Learning*, 2020.

A CUBE GRASPING EXPERIMENT DETAILS

A.1 ENVIRONMENT DETAILS

For the cube grasping experiments in Section 3, we investigate three types of distribution shifts. The experiment variants for DAgger and DrQ are summarized in Table 3. The DAC experiments featured a subset of these conditions explained in the caption of Figure 3. Figures 6, 7, and 8 visualize each type of distribution shift.

Table 3: Variants of the cube grasping environment with distribution shifts used for the DAgger and DrQ experiments. All task variants include initial object position and initial end-effector position randomization that is consistent across train and test. Table textures are from the describable textures dataset (DTD) (Cimpoi et al., 2014).

	train	test
table height	$z_{\text{shift}} = 0$	$z_{\text{shift}} \in \{-0.10, -0.05, +0.05, +0.10\}$
distractor objects	1 red, 1 green, 1 blue	3 of color $\in$ {red, green, blue, brown, white, black}
table texture	texture $\in$ 5 DTD textures	texture $\in$ 20 held-out DTD textures

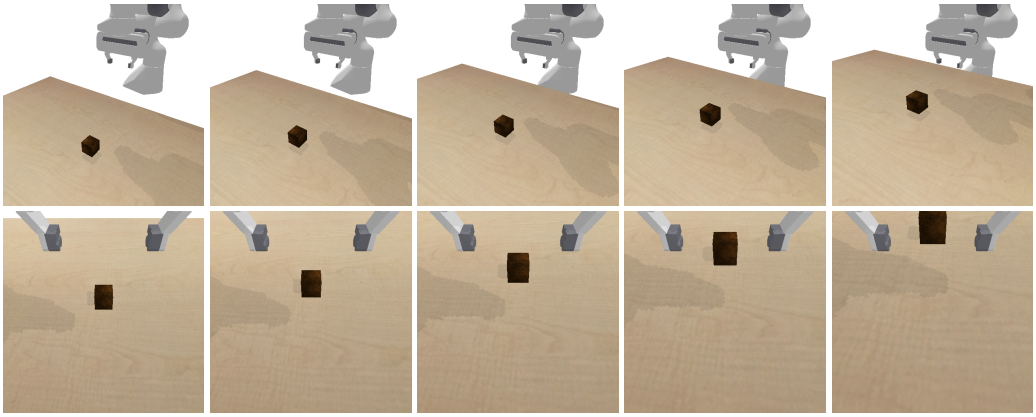

Figure 6: Visualization of the table height distribution shift used in the cube grasping experiments. From left to right, z_{shift} is $-0.10, -0.05, 0, +0.05, +0.10$. The top and bottom rows contain the third-person and hand-centric perspectives, respectively. Positions of the cube and end-effector are not randomized in this visualization for the sake of clarity.

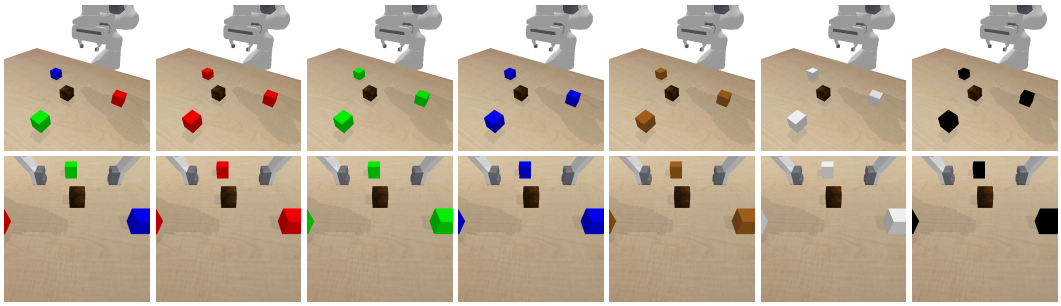

Figure 7: Visualization of the distractor objects distribution shift used in the cube grasping experiments. From left to right, we have "mix" (1 red, 1 green, 1 blue), 3 red, 3 green, 3 blue, 3 brown, 3 white, and 3 black. The top and bottom rows contain the third-person and hand-centric perspectives, respectively. Positions of the cubes and end-effector are not randomized in this visualization for the sake of clarity.

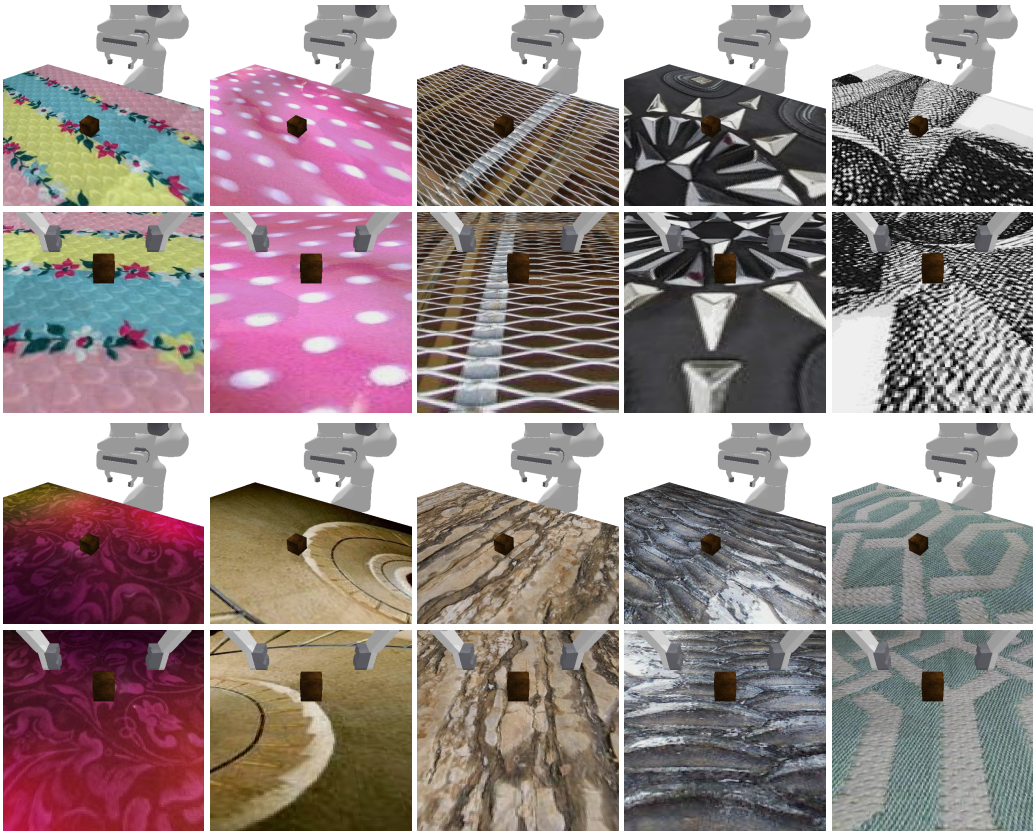

Figure 8: Visualization of the table textures distribution shift used in the cube grasping experiments. The top two rows contain the third-person and hand-centric perspectives of the five table textures used during training for DAgger and DrQ, and the bottom two rows contain the perspectives of five held-out textures used at test time (out of twenty total held-out textures). Positions of the cube and end-effector are not randomized in this visualization for the sake of clarity. The textures were acquired from the describable textures dataset (DTD) (Cimpoi et al., 2014).

A.2 ALGORITHMS

The dataset aggregation (DAgger) algorithm proposed by Ross et al. (2011) is an iterative online algorithm for training an imitation learning policy. In each iteration i (which we call a "DAgger round"), the current policy π_i is run to sample a set of trajectories, and an expert policy π^* is used to label each of the visited states with an optimal action. These labeled trajectories are aggregated into a dataset $\mathcal{D}$ that grows in size over the DAgger rounds, and the imitation learning policy $\hat{\pi}_i$ is trained on the entire $\mathcal{D}$ for some number of epochs before repeating the above procedure in the next iteration. The trajectory-generating policy π_i is often modified such that in earlier DAgger rounds the expert policy π^* is utilized more heavily than the imitation learning policy $\hat{\pi}_i$ when collecting new trajectories, i.e. $\pi_i = \beta_i \pi^* + (1 - \beta_i)\hat{\pi}_i$, where β_i is typically annealed over time (e.g., linearly from 1 to 0 over the DAgger rounds).

The Data-regularized Q (DrQ) algorithm proposed by Kostrikov et al. (2020) is a model-free, off-policy, actor-critic reinforcement learning algorithm that applies image augmentation techniques commonly used in computer vision (primarily random shifts) to input images, along with regularizations of the Q target and function, such that deep neural network-based agents can be trained effectively from pixels. The original DrQ paper uses soft actor-critic (Haarnoja et al., 2018) and DQN (Mnih et al., 2013) as backbones; we use the soft actor-critic version in our experiments because the cube grasping action space is continuous.

The discriminator actor-critic algorithm (DAC) was proposed in Kostrikov et al. (2018) and is an off-policy version of the generative adversarial imitation learning (GAIL) method (Ho & Ermon, 2016). Unlike Kostrikov et al. (2018) we use a deterministic reinforcement learning algorithm similar to that of Fujimoto et al. (2018), as we find this helps stability. To scale the method to image observations, we apply similar augmentation techniques as in Kostrikov et al. (2020).

A.3 MODEL ARCHITECTURES

For DAgger in the cube grasping experiments discussed in Section 3, we feed the 84×84 images into a ResNet-18 convolutional image encoder (He et al., 2016) trained from scratch, with the final classification layer replaced by a linear layer that outputs a 64-dimensional representation. We concatenate proprioceptive information (3D end-effector position relative to the robot base, 1D gripper width, and a Boolean contact flag for each of two gripper "fingers") to the image representation, and the result is passed into feedforward policy and value networks with two hidden layers of 32 units each.

For DrQ, we use the original actor-critic DrQ model proposed by Kostrikov et al. (2020), except for one modification: we concatenate proprioceptive information (3D end-effector position relative to the robot base, 1D gripper width, and a Boolean contact flag for each of two gripper "fingers") to the flattened image representation before feeding it into the actor and critic networks.

For the DAC algorithm we use the same convolutional architectures as Kostrikov et al. (2018). The convolutional encoder is shared between the discriminator, actor and critic. We use additional MLP heads with capacities 128, 256 and 256 respectively for those components, as we empirically found that lower-capacity networks decrease the likelihood of overfitting to spurious features.

A.4 HYPERPARAMETERS

The DAgger, DrQ, and DAC hyperparameters used in the cube grasping experiments are listed in Tables 4, 5, and 6, respectively.

Table 4: The default hyperparameters used for DAgger in the cube grasping environment.

parameter	setting
num. DAgger rounds	6
num. new episodes per round	200
num. epochs per round	15
batch size	256
β schedule (% time expert policy is used)	linear anneal from 1 to 0 over 6 rounds
learning rate	10^{-3}

Table 5: The default hyperparameters used for DrQ in the cube grasping environment.

parameter	setting
replay buffer capacity	10^5
action repeat	2
seed steps	1000
n-step returns	3
mini-batch size	128
discount γ	0.99
optimizer	Adam
learning rate	10^{-3}
critic target update frequency	2
critic Q-function soft-update rate τ	0.01
actor update frequency	2
actor log stddev. bounds	$[-10, 2]$
init. temperature	0.1
features dim.	50
hidden dim.	1024

Table 6: The default hyperparameters used for DAC in the cube grasping environment.

parameter	setting
replay buffer capacity	15×10^3
action repeat	1
seed steps	200
mini-batch size	512
discount γ	0.99
optimizer	Adam
learning rate	10^{-3}
actor	deterministic
critic Q-function soft-update rate τ	0.01
features dim.	64
discriminator hidden dim.	128
actor hidden dim.	256
critic hidden dim.	256

A.5 MINOR DISCREPANCIES BETWEEN ALGORITHMS

Due to implementation idiosyncrasies, there are minor discrepancies in how each algorithm processes environment observations. Following Kostrikov et al. (2020), for DrQ and DAC-DrQ observations are "frame-stacked" with three time steps' observations. This was not done for DAgger. Proprioceptives are used for DAgger and DrQ but not for DAC-DrQ. We take the position that these differences increase the generalizability of the trends we observe. We emphasize that the target effect under consideration is O_h vs. O_3 in each setting.

B META-WORLD EXPERIMENT DETAILS

B.1 INDIVIDUAL TASK DESCRIPTIONS

In this section, we explain the tasks that the agents must learn to accomplish in the six Meta-World environments discussed in Section 4.2 and visualized in Figure 4. We also explain why each task falls under a certain level of hand-centric observability. For details regarding the train and test distributions, see Appendix B.2.

- handle-press-side: The goal is to press the handle fully downwards. Hand-centric observability is high because the handle is well aligned with the hand-centric camera's field of view.
- button-press: The goal is to push the button fully inwards. Hand-centric observability is high because the button is well in view of the hand-centric camera, and the button remains largely in view as the gripper approaches and presses it.
- soccer: The goal is to push or pick-and-place the ball into the center of the goal net. Hand-centric observability is moderate because when the gripper approaches the ball, the observability of the goal net is appreciably reduced.
- peg-insert-side: The goal is to lift the peg and insert it into the hole in the target box. Hand-centric observability is moderate because when the gripper approaches the peg, the observability of the target box is appreciably reduced.
- reach-hard: The goal is to move the gripper to the green goal site, which is initialized either to the left or right side of the gripper with equal probability (see Figure 9). Hand-centric observability is low because the gripper is initialized at the same height as the goal, and we restrain the gripper from moving vertically. Effectively, if given just the hand-centric perspective's observations, the agent does not know in which direction to move the gripper in the beginning of an episode.
- peg-insert-side-hard: The goal is the same as in peg-insert-side, but like the green goal site in reach-hard, the peg in this environment is initialized either to the left or right side of the gripper with equal probability (see Figure 9). Hand-centric observability is low because the gripper is initialized at the same height as the peg such that the peg is not initially visible to the hand-centric view (though we do *not* prohibit vertical movement of the gripper as in reach-hard, since this would make the peg insertion part of the task impossible), and also because the peg and target box are initialized much farther apart than they are in peg-insert-side (thus, the target box is completely out of view as the agent approaches and grasps the peg).

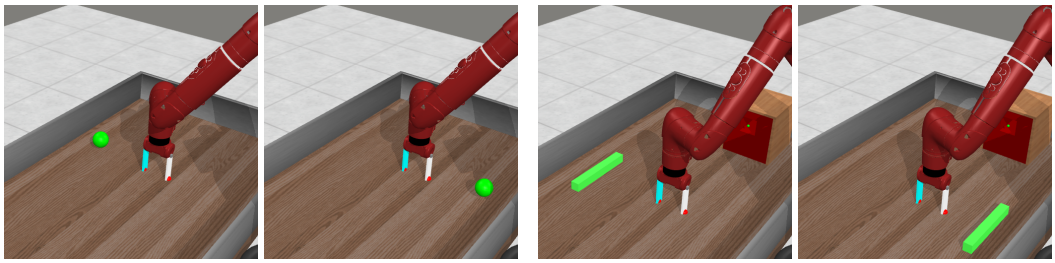

Figure 9: Visualizations of the two sides that the green goal site or peg can be initialized to in the reach-hard and peg-insert-side-hard tasks in Meta-World, respectively. One of the two sides is chosen via "coin flip" at the beginning of each episode.

B.2 TRAIN AND TEST DISTRIBUTIONS

At training time, initial positions of the objects in the Meta-World tasks are randomly sampled within some small range. At test time, initial positions are sampled from a distribution that is completely disjoint from the training distribution, such that we test on out-of-distribution initial object positions. To implement this, at test time we resample the set of initial object positions if *any* of the positions overlaps with its train-time distribution. The full set of train-time and test-time initial object positions is shown in Table 7. For visualizations, see Figure 10.

Table 7: The distributions of the initial object positions used in the six Meta-World environments. At training time, we use the "narrow" initial object positions. At test time, we use the set difference between the "narrow" and "wide" initial object positions, i.e. we repeatedly resample from "wide" until none of the objects in the environment lie in the "narrow" distribution. As a result, the train- and test-time distributions are disjoint. The range of positions for each object is given as a pair of coordinates: $(x_{\text{low}}, y_{\text{low}}, z_{\text{low}})$ and $(x_{\text{high}}, y_{\text{high}}, z_{\text{high}})$.

task	"narrow" init. obj. positions (x, y, z)	"wide" init. obj. positions (x, y, z)
handle-press-side	$\text{handle}_{\text{low}} : (-0.35, 0.55, -0.001)$ $\text{handle}_{\text{high}} : (-0.15, 0.65, 0.001)$	$\text{handle}_{\text{low}} : (-0.55, 0.4, -0.001)$ $\text{handle}_{\text{high}} : (-0.15, 0.8, 0.001)$
button-press	$\text{button}_{\text{low}} : (-0.2, 0.85, 0.115)$ $\text{button}_{\text{high}} : (0, 0.9, 0.115)$	$\text{button}_{\text{low}} : (-0.4, 0.75, 0.115)$ $\text{button}_{\text{high}} : (0.2, 0.9, 0.115)$
soccer	$\text{ball}_{\text{low}} : (-0.2, 0.6, 0.03)$ $\text{ball}_{\text{high}} : (0., 0.7, 0.03)$ $\text{goal}_{\text{low}} : (-0.2, 0.8, 0.0)$ $\text{goal}_{\text{high}} : (0., 0.9, 0.0)$	$\text{ball}_{\text{low}} : (-0.3, 0.6, 0.03)$ $\text{ball}_{\text{high}} : (0.1, 0.7, 0.03)$ $\text{goal}_{\text{low}} : (-0.3, 0.8, 0.0)$ $\text{goal}_{\text{high}} : (0.1, 0.9, 0.0)$
peg-insert-side	$\text{peg}_{\text{low}} : (.05, 0.55, 0.02)$ $\text{peg}_{\text{high}} : (.15, 0.65, 0.02)$ $\text{goal}_{\text{low}} : (-0.325, 0.5, -0.001)$ $\text{goal}_{\text{high}} : (-0.275, 0.6, 0.001)$	$\text{peg}_{\text{low}} : (.0, 0.5, 0.02)$ $\text{peg}_{\text{high}} : (.2, 0.7, 0.02)$ $\text{goal}_{\text{low}} : (-0.35, 0.4, -0.001)$ $\text{goal}_{\text{high}} : (-0.25, 0.7, 0.001)$

reach-hard	if goal is on left of gripper:
	$\text{goal}_{\text{low}} : (-0.2, 0.85, 0.05)$
	$\text{goal}_{\text{high}} : (-0.2, 0.85, 0.05)$
	if goal is on right of gripper:
	$\text{goal}_{\text{low}} : (-0.2, 0.35, 0.05)$
	$\text{goal}_{\text{high}} : (-0.2, 0.35, 0.05)$
		if goal is on left of gripper:
		$\text{goal}_{\text{low}} : (-0.5, 0.9, 0.05)$
		$\text{goal}_{\text{high}} : (0.1, 0.9, 0.05)$
		if goal is on right of gripper:
		$\text{goal}_{\text{low}} : (-0.5, 0.3, 0.05)$
		$\text{goal}_{\text{high}} : (0.1, 0.3, 0.05)$

peg-insert-side-hard	if peg starts on left of gripper:
	$\text{peg}_{\text{low}} : (-0.025, 0.85, 0.02)$
	$\text{peg}_{\text{high}} : (0.025, 0.85, 0.02)$
	$\text{goal}_{\text{low}} : (-0.525, 0.5, -0.001)$
	$\text{goal}_{\text{high}} : (-0.525, 0.6, 0.001)$
	if peg starts on right of gripper:
	$\text{peg}_{\text{low}} : (-0.025, 0.35, 0.02)$
	$\text{peg}_{\text{high}} : (0.025, 0.35, 0.02)$
	$\text{goal}_{\text{low}} : (-0.525, 0.5, -0.001)$
	$\text{goal}_{\text{high}} : (-0.525, 0.6, 0.001)$
		if peg starts on left of gripper:
		$\text{peg}_{\text{low}} : (-0.3, 0.85, 0.02)$
		$\text{peg}_{\text{high}} : (0.1, 0.85, 0.02)$
		$\text{goal}_{\text{low}} : (-0.525, 0.3, -0.001)$
		$\text{goal}_{\text{high}} : (-0.525, 0.75, 0.001)$
		if peg starts on right of gripper:
		$\text{peg}_{\text{low}} : (-0.3, 0.35, 0.02)$
		$\text{peg}_{\text{high}} : (0.1, 0.35, 0.02)$
		$\text{goal}_{\text{low}} : (-0.525, 0.3, -0.001)$
		$\text{goal}_{\text{high}} : (-0.525, 0.75, 0.001)$

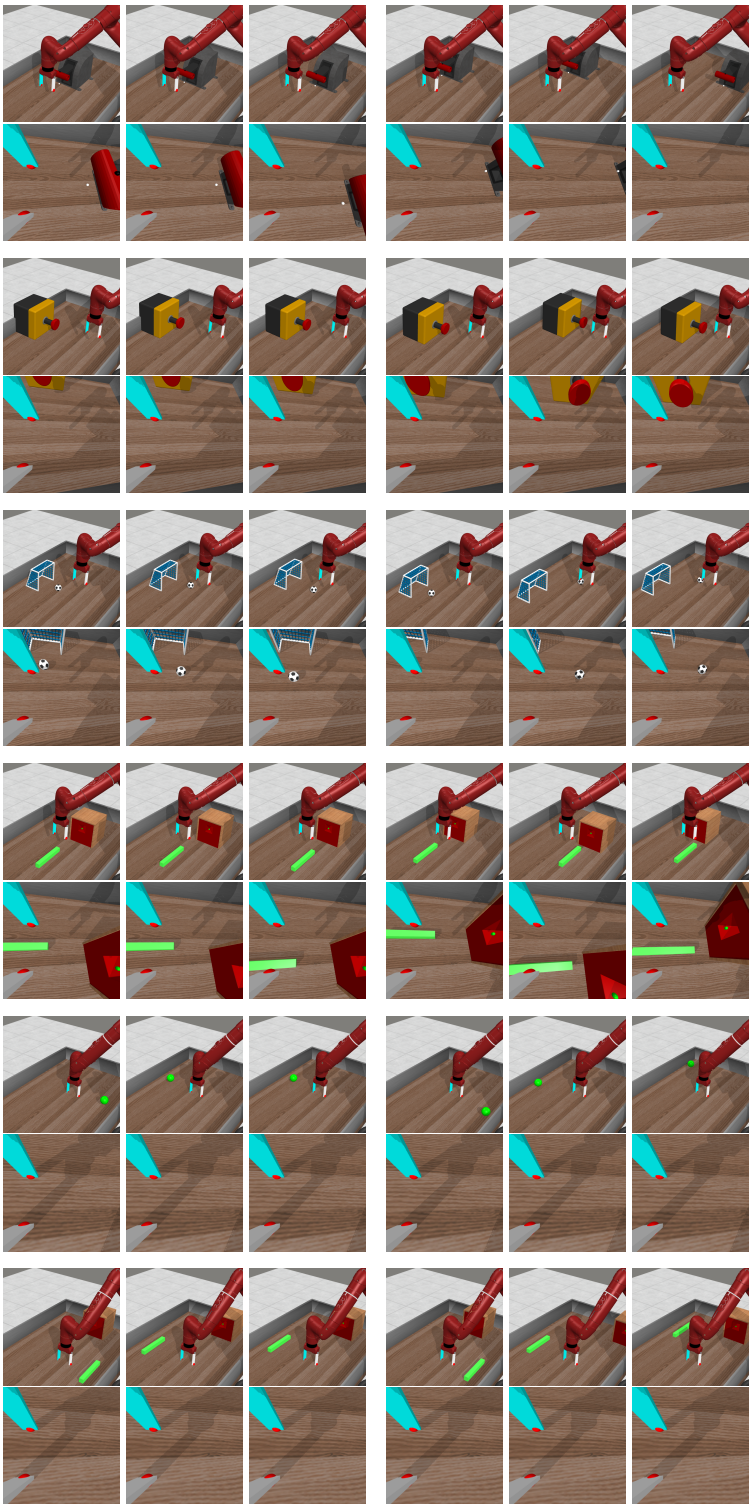

Figure 10: Visualization of the train and test distributions in the six Meta-World environments used in the experiments in Section 4. The three columns in the left half of the figure show three sets of initial object positions randomly sampled from the training distribution; the three columns in the right half correspond to the test distribution. From top to bottom are handle-press-side, button-press, soccer, peg-insert-side, reach-hard, and peg-insert-side-hard. Both the third-person and hand-centric perspectives are shown for each random initialization.

B.3 DrQ-v2

DrQ-v2 (Yarats et al., 2021) is a state-of-the-art vision-based actor-critic reinforcement learning algorithm that uses deep deterministic policy gradients (DDPG) (Lillicrap et al., 2015) as a backbone (whereas DrQ-v1 by Kostrikov et al. (2020) uses soft actor-critic). The DrQ-v2 model includes:

- a convolutional image encoder f_ξ that outputs representation $\mathbf{z} = f_\xi(\mathrm{aug}(\mathbf{o}))$ given frame-stacked image observations $\mathbf{o}$ and a data augmentation function aug,
- two critic networks Q_{θ_k} that output Q-values $Q_{\theta_k}(\mathbf{z}, \mathbf{a}), k = 1, 2$, à la clipped double Q-learning (Fujimoto et al., 2018),
- and an actor network π_ϕ that outputs action $\mathbf{a} = \pi_\phi(\mathbf{z}) + \epsilon, \epsilon \sim \mathcal{N}(0, \sigma^2)$, with σ^2 annealed over the course of training.

The individual critic losses are given by

$$\mathcal{L}_k = \mathbb{E}_{\tau \sim \mathcal{D}} \left[\left(Q_{\theta_k}(\mathbf{z}, \mathbf{a}) - y \right)^2 \right], \; k = 1, 2 \tag{2}$$

where $\tau = (\mathbf{o}_t, \mathbf{a}_t, r_{t:t+n-1}, \mathbf{o}_{t+n})$ is a sample from replay buffer $\mathcal{D}$ and y is the temporal difference target estimated via n-step returns:

$$y = \sum_{i=0}^{n-1} \gamma^i r_{t+i} + \gamma^n \min_{k \in \{1,2\}} Q_{\bar{\theta}_k}(\mathbf{z}_{t+n}, \mathbf{a}_{t+n}) \tag{3}$$

for slow-moving critic weights $\bar{\theta}_1$, $\bar{\theta}_2$. We omit presentation of the actor loss as we do not need to modify it; in DrQ-v2, only gradients from the critic loss are used to update the weights of the encoder(s).

In terms of the model architecture used in the experiments discussed in Section 4, we use the original DrQ-v2 architecture, except for two modifications: first, we concatenate proprioceptive information (3D end-effector position and 1D gripper width) to the flattened image representation before feeding it into the actor and critic networks. Second, when using two perspectives at the same time (e.g., hand-centric and third-person), we use two separate image encoders that do not share weights. The two representations are concatenated together (along with the proprioceptive information) and fed into the actor and critic networks. The dimensionality of each encoder's output representation is preserved, thereby doubling the dimensionality of the final combined image representation.

B.4 Ablation Experiments Details

Figure 11 presents the train and test curves of the ablation experiments presented in Section 4.3. Figure 12 contains illustrations of the second third-person perspective used in $\pi \circ O_{3'+3+p} + \text{VIB}(\mathbf{z}_3)$.

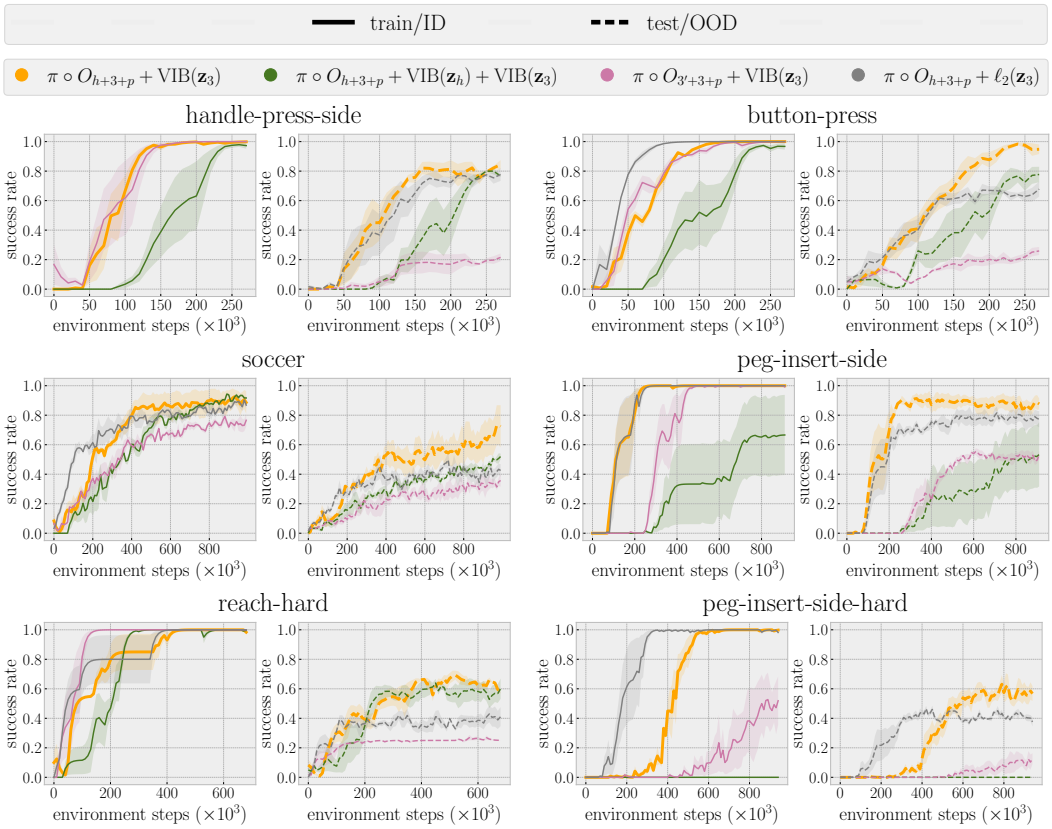

Figure 11: Ablation studies on $\pi \circ O_{h+3+p} + \text{VIB}(\mathbf{z}_3)$ in Meta-World. Shaded regions indicate the standard error of the mean over three random seeds. Note that for $\pi \circ O_{h+3+p} + \text{VIB}(\mathbf{z}_h) + \text{VIB}(\mathbf{z}_3)$ in peg-insert-side, DrQ-v2 training did not converge within the specified number of training steps for one of three random seeds (hence the larger shaded regions and the lower out-of-distribution generalization performance). In addition, for $\pi \circ O_{h+3+p} + \text{VIB}(\mathbf{z}_h) + \text{VIB}(\mathbf{z}_3)$ in peg-insert-side-hard, DrQ-v2 training did not converge for any of the three seeds.

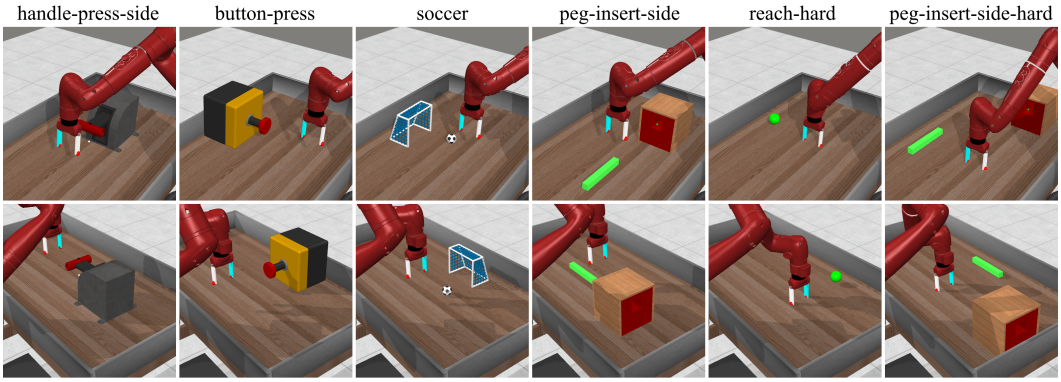

Figure 12: Visualizations of the two third-person perspectives used in the ablation agent $\pi \circ O_{3'+3+p} + \text{VIB}(\mathbf{z}_3)$ discussed in Section 4.3. The top row contains the original third-person perspective; the bottom row contains the second third-person perspective used only in the ablation.

B.5 HYPERPARAMETERS

We present the DrQ-v2 hyperparameters used in the Meta-World experiments in Table 8. The configuration is largely identical to the one used in the original DrQ-v2 algorithm (Yarats et al., 2021).

Table 8: The hyperparameters used for DrQ-v2 in the six Meta-World environments. The lower half of the table presents the hyperparameters that are specific to the regularization methods and ablation agents.

parameter	setting
replay buffer capacity	100,000 for {handle-press-side, button-press, reach-hard}; 400,000 for all other environments
action repeat	2
frame stack	3
seed frames	4000
exploration steps	2000
n-step returns	3
mini-batch size	256
discount γ	0.99
optimizer	Adam
learning rate	10^{-4}
agent update frequency	2
critic Q-function soft-update rate τ	0.01
features dim.	50
hidden dim.	1024
exploration stddev. clip	0.3
exploration stddev. schedule	linear$(1.0, 0.1, 500000)$
weight β_3 of KL div. term in $\pi \circ O_{h+3+p} + \text{VIB}(\mathbf{z}_3)$	500 for {soccer, peg-insert-side-hard}; 10 for all other environments
weights β_h, β_3 of KL div. terms in $\pi \circ O_{h+3+p} + \text{VIB}(\mathbf{z}_h) + \text{VIB}(\mathbf{z}_3)$	β_h: 0.1 for {button-press, reach-hard, soccer}; 0.001 for all other environments β_3: same as β_3 of KL div. term in $\pi \circ O_{h+3+p} + \text{VIB}(\mathbf{z}_3)$
weight β_3 of KL div. term in $\pi \circ O_{3'+3+p} + \text{VIB}(\mathbf{z}_3)$	0 for handle-press-side; 500 for soccer; 1 for all other environments
weight α_3 of ℓ_2 reg. term in $\pi \circ O_{h+3+p} + \ell_2(\mathbf{z}_3)$	10^8 for all environments

C MISCELLANEOUS DETAILS

We applied an exponentially weighted moving average filter on the data for DrQ in Figure 2 ($\alpha = 0.6$), for DAC in Figure 3 ($\alpha = 0.3$), and for DrQ-v2 in Figures 5 and 11 ($\alpha = 0.5$) to smoothen the train and test curves for increased readability. The smoothing factor α lies in the range $[0, 1]$, where values closer to 0 correspond to more smoothing.